COOLING, GRAVITY, AND GEOMETRY: FLOW-DRIVEN MASSIVE CORE FORMATION

FABIAN HEITSCH,[1] LEE W. HARTMANN,[1] ADRIANNE D. SLYZ,[2] JULIEN E. G. DEVRIENDT,[3] AND ANDREAS BURKERT[4]

ABSTRACT

We study numerically the formation of molecular clouds in large-scale colliding flows including self-gravity. The models emphasize the competition between the effects of gravity on global and local scales in an isolated cloud. Global gravity builds up large-scale filaments, while local gravity, triggered by a combination of strong thermal and dynamical instabilities, causes cores to form. The dynamical instabilities give rise to a local focusing of the colliding flows, facilitating the rapid formation of massive protostellar cores of a few hundred $M_\odot$. The forming clouds do not reach an equilibrium state, although the motions within the clouds appear to be comparable to virial. The self-similar core mass distributions derived from models with and without self-gravity indicate that the core mass distribution is set very early on during the cloud formation process, predominantly by a combination of thermal and dynamical instabilities rather than by self-gravity.

Subject headings: gravity — instabilities — ISM: clouds — methods: numerical — stars: formation — turbulence

1. RAPID STAR FORMATION

There is increasing evidence that star formation in the solar neighborhood follows rapidly upon molecular cloud formation (Hartmann et al. 2001; Ballesteros-Paredes & Hartmann 2007 and references therein). This evidence suggests that the density enhancements in which stars form are produced during the cloud formation phase; thus, understanding cloud formation is essential to understanding star formation. Moreover, it appears that non-linear density perturbations need to arise quite early in cloud formation, as massive, finite molecular clouds are highly susceptible to large-scale gravitational collapse, which could overwhelm small, stellar mass fragmentation (Burkert & Hartmann 2004). While several investigations have adopted various assumed forms of initial and/or driven turbulent motions to produce the necessary small-scale structure (Klessen & Burkert 2000; Padoan & Nordlund 2002; Bate et al. 2002, 2003), it is preferable to have these structures arise naturally. Thus, a close look at instabilities in cloud formation that could lead to strong density fluctuations is needed.

Ballesteros-Paredes et al. (1999a) and Hartmann et al. (2001) proposed that cloud formation as the result of a pileup of material by large-scale flows is an essential mechanism for explaining the "crossing time problem," i.e., the observation that the typical age spreads in the stellar populations of many large star-forming regions are often substantially smaller than the lateral crossing timescales; in the large-scale flow picture, no information is transmitted laterally, i.e., perpendicular to the large-scale flow. This picture works only if star formation follows closely upon molecular gas formation. Expanding H II regions, supernova bubbles, and spiral density waves are all obvious candidates for large-scale supersonic flows that can sweep up material, and there is considerable direct observational evidence for rapid star formation in these environments (Hartmann et al. 2001 and references

therein). Thus, a plausible place to look for stellar core-forming instabilities is in the postshock material of the large-scale flows.

Several numerical studies relevant to this problem have now been undertaken (see the discussions of the literature in Heitsch et al. 2006 and Vázquez-Semadeni et al. 2007). These calculations typically assume converging flows in order to keep the shocked gas within the computational volume, but this can easily be extended to describe a more generic situation by recasting the problem in the rest frame of the shock(s). These models overcome the limitations of previous turbulent fragmentation models (see the review by Mac Low & Klessen 2004) by avoiding ad hoc assumptions about the source of turbulence and boundary conditions. Indeed, the converging flow models demonstrate with ease that flows provide a natural mechanism for the generation of structure and turbulence in clouds (Audit & Hennebelle 2005; Heitsch et al. 2005; Vázquez-Semadeni et al. 2006; Heitsch et al. 2006; Hennebelle et al. 2007; Hennebelle & Audit 2007).

Although this study is motivated by the scenario of molecular clouds being transient entities (Ballesteros-Paredes et al. 1999a), forming and dispersing in background flows within a few free-fall times, the results presented here are not restricted to this scenario. Colliding flows can appear even in large-scale gravitational instabilities, linking our models to the alternative scenario of giant molecular clouds that live for substantially longer than only a few free-fall times. The issue of cloud lifetimes is currently a matter of debate (e.g., Krumholz & Tan 2007; Elmegreen 2007; McKee & Ostriker 2007), and it seems to depend strongly on the galactic environment (Hartmann et al. 2001; Heitsch et al. 2006). For reasons discussed in § 5, our models cannot predict cloud lifetimes. Thus, the emphasis of this study is on the *onset* of star formation.

The purpose of this study is to compare the fragmentation processes in simulated converging flows with and without self-gravity in order to show that the rapid onset of star formation is pretty much unavoidable within the scenario in which molecular clouds form in converging flows. Recently, Vázquez-Semadeni et al. (2007) presented a study of star formation in clouds formed by colliding flows, emphasizing the long-term evolution of the system. Here we focus more on the initial development of the cloud, discussing the consequences of cooling, cloud geometry, and gravity for the star formation process.

[1] Department of Astronomy, University of Michigan, 500 Church Street, Ann Arbor, MI 48109-1042.

[2] Oxford University, Astrophysics, Denys Wilkinson Building, Keble Road, Oxford, OX1 3RH, United Kingdom.

[3] Université Claude Bernard Lyon 1, CRAL, Observatoire de Lyon, 9 Avenue Charles André, 69561 St-Genis Laval Cedex; CNRS, UMR 5574; ENS Lyon, France.

[4] Universitäts-Sternwarte München, Scheinerstrasse 1, 81679 München, Germany.

Both cooling and gravity are fragmentation agents, with the difference that gravity can be relevant on all scales that surpass the Jeans length, while the isobaric condensation mode of the thermal instability (Field 1965) is limited to scales set by the sound speed and the cooling time, $\lambda_c = c_s \tau_c$ (e.g., Burkert & Lin 2000; Hennebelle & Audit 2007). Thus, in the early stages of cloud formation, when only a little mass has accumulated, the thermal instability is the dominant fragmentation agent.

Nonlinear density perturbations collapse at a higher rate than that of the global cloud (Burkert & Hartmann 2004), thus allowing stars to form locally before the wholesale collapse of the cloud. We find that the strong dynamical and thermal instabilities generate nonlinear density perturbations for rapid *local* collapse, while still allowing for the global buildup of the cloud.

The physics and methods are summarized in § 2, followed by the model results in § 3. Readers solely interested in a discussion of the results and their consequences should directly proceed to §§ 4 and 5.

2. PHYSICS AND METHODS

Our study focuses on the effects of global versus local gravity on the one hand and on the rapid generation of substructure in the colliding flows on the other. Since we are interested in global gravitational effects, we cannot use the periodic boundary conditions of earlier turbulent fragmentation studies (e.g., Klessen et al. 2000; Heitsch et al. 2001; Padoan et al. 2001; Gammie et al. 2003; Vázquez-Semadeni et al. 2005). Neither will we generate or drive turbulence by imposing a randomly chosen velocity or density field, but instead, we will rely on turbulence generated by the dynamical instabilities arising from the collisions of the flows.

2.1. *The Models*

We ran four models, whose parameters are listed in Table 1. All models are run on a fixed grid with the instreaming gas flowing along the x-direction, entering the domain at the (y, z)-planes. To trigger the fragmentation of the (otherwise plane-parallel) interaction region, we perturb the collision interface. We chose the perturbations of the collision interface from a random distribution of amplitudes in Fourier space with a top-hat distribution restricted between wavenumbers $k = 1$ and 4.

Model Gs (for "gravity in shell") can be interpreted as colliding continuous gas streams in spiral shocks (e.g., Tilanus & Allen [1990] for observational evidence and Dobbs & Bonnell [2007] for numerical models), or as a close-up view of two expanding and colliding supershells in the LMC. The collision interface is plane-parallel, except for the imposed perturbations. Material is free to leave the box in the lateral (i.e., perpendicular to the inflow) directions. In models Gf1 and Gf2 (for "gravity in finite cloud"), we restrict the inflow to a cylinder of elliptical cross section with an ellipticity of 3.3 and a major axis of 80% of the (transverse) box size, mimicking two colliding gas streams in a more general geometry. Again, the collision interface is perturbed. The motivation here is to generate one finite cloud in order to study global gravitational effects. Finally, model Hf1 is a nongravitating version of model Gf1, to compare the role of gravity versus that of the thermal instability for the fragmentation of the gas streams.

The inflow density in all models is $n_0 = 3$ cm^{-3} at a temperature of $T_0 = 1800$ K and an inflow velocity of 7.9 km s^{-1}, corresponding to a Mach number of $\mathcal{M} = 1.5$. The flows are initially in thermal equilibrium. The models start at time $t = 0$ with the collision of the two flows. For models with spatially constrained inflows (Hf1, Gf1, and Gf2), the fluid is at rest everywhere except in the colliding cylinders.

TABLE 1
MODEL PARAMETERS

Name (1)	$n_x n_y n_z$ (2)	$L_x L_y L_z$ (pc) (3)	Gravity (4)	t_{end} (Myr) (5)	η (pc) (6)
Hf1	256×512^2	22×44^2	No	14.5	2.2
Gf1	256×512^2	22×44^2	Yes	14.5	2.2
Gf2	256×512^2	22×44^2	Yes	14.5	4.4
Gs	256^3	44^3	Yes	16.0	2.2

NOTES.—Col. (1): Model name. Col. (2): Resolution. Col. (3): Physical grid size. Col. (4): Gravity. Col. (5): End time of run. Col. (6): Amplitude of interface displacement.

The finite cloud models Gf1, Gf2, and Hf1 have a grid cell size of $\Delta L = 8.6 \times 10^{-2}$ pc, while model Gs has one of $\Delta L = 1.7 \times 10^{-1}$ pc (Table 1). We note that this does *not* constitute the physical resolution power of the simulation. At minimum, the stencils (i.e., the support points) used for the higher order reconstruction of the fluid states at the cell wall will render the cells within one stencil not independent. In other words, conclusions should not be drawn from structures of four cells or less of linear size. Thus, we use only cores with 64 or more cells for analysis.

2.2. *Boundary Conditions*

The x-boundaries are partly or entirely defined as inflow boundaries, depending on the model. Indeed, the inflow is either defined over the whole (y, z)-plane (model Gs) or within an elliptical surface (models Hf1, Gf1, and Gf2: see § 2.1 for details). The y- and z-boundaries, as well as the parts of the x-boundaries that are not occupied by the inflow in models Hf1, Gf1, and Gf2, are open, meaning that material is free to leave the simulation domain through these boundaries. This is bound to cause trouble once material tries to "come back" during the later stages of the simulation (note that this material is not actually coming back, but that it is the result of the extrapolation of the properties of the last active cells; i.e., material with the properties of the last active cell layer within the domain will try to enter the domain). This inevitably will happen once global gravity dominates over the overpressurized material shooting out of the flow-collision region. However, the "reentering" material does not reach the central cloud region within the simulation time, and in any case it contributes only a negligible amount to the total mass within the box.

The situation becomes more critical once material is leaving the simulation domain in the x-direction; i.e., once it is moving against the inflow. Since the bounding shocks (and the cooling) will set the density and the temperature of the postshock gas, the physical state of the gas will be undefined once the bounding shocks move off the grid. This will render the "returning" material into an essentially hydrodynamically inconsistent state. Thus, once material encounters the x-boundaries, the simulation needs to be stopped.

In model Gs, the inflow velocities are slightly reduced at the edges of the domain, mimicking the velocity profile of an expanding shell of material driven by two sources at a distance of approximately 100 pc to the left and to the right of the midplane of the simulation domain. This reduces the amount of material collected at the edges of the domain and thus limits the edge effects due to gravity at later stages of the simulation.

2.3. *Hydrodynamics and Atomic Line Coolants*

As in our previous studies of colliding flows, we used the higher order gas-kinetic grid method Proteus (Prendergast & Xu

1993; Slyz & Prendergast 1999; Heitsch et al. 2004; Slyz et al. 2005; Heitsch et al. 2006, 2007), which gives us full control of viscosity and heat conduction. The code evolves the Navier-Stokes equations in their conservative form to second order in time and space. The hydrodynamical quantities are updated in time-unsplit form.

The heating and cooling rates are restricted to optically thin atomic lines, following Wolfire et al. (1995). Dust extinction becomes important above column densities of $N(\text{H I}) \approx 1.2 \times 10^{21} \text{ cm}^{-2}$, which are only reached in the densest regions modeled. Thus, we use the unattenuated UV radiation field for grain heating (Wolfire et al. 1995), expecting substantial uncertainties in cooling rates only for the densest regions. The ionization degree is derived from a balance between ionization by cosmic rays and recombination, assuming that Lyα photons are directly reabsorbed. Numerically, heating and cooling is implemented iteratively as a source term for the internal energy e of the form

$$\partial_t e = n\Gamma(T) - n^2\Lambda(T) \text{ [erg cm}^{-3} \text{ s}^{-1}]. \quad (1)$$

Here Γ is the heating contribution (mainly photoelectric heating from grains) and $n\Lambda$ is the cooling contribution (mainly due to the C II hyperfine structure line at 158 μm). Since the cooling and heating prescription has to be added outside the flux computations, it lowers the time order of the scheme. To speed up the calculations, equation (1) is tabulated on a 2048^2 grid in density and temperature. For each cell and iteration, the actual energy change is then bilinearly interpolated from this grid.

The cores forming due to gravitational collapse reach densities of a few times 10^5 cm^{-3}, far beyond the applicable range of our cooling curve. Strictly speaking, we should therefore extend the cooling curve to include molecular lines at high densities. However, our cooling curve reaches an equilibrium temperature of approximately 12 K for $n > 10^3 \text{ cm}^{-3}$, which is close enough to a realistic temperature for molecular cores. Since we cannot resolve the core structure anyway, we chose to stick to this simplified treatment.

The cooling curve is limited to densities of $n \leq 10^5 \text{ cm}^{-3}$ to prevent a catastrophic collapse that would be generated by a sub-isothermal effective equation of state. The sudden reversal to an adiabatic equation of state helps to limit the densities and prevents numerical artifacts caused by single very high density cells. However, this stiffening of the equation of state, if introduced at too-low densities, could stabilize the cores, prevent their fragmentation, and render them more prone to dispersion. We experimented with the density threshold $n_{\max}$ and found that a value of $n_{\max} = 10^5 \text{ cm}^{-3}$ prevents the runaway collapse while allowing the cores to remain small (and dense) enough to stay gravitationally bound once they have formed. See § 3.4 for a discussion of the resolution limits.

2.4. Gravity

Self-gravity is implemented as an external source term in time-unsplit form. The Poisson equation is solved via a nonperiodic Fourier solver, using the (MPI-parallelized) fftw (Fastest Fourier Transform in the West) libraries. We tested this against direct summation to ensure that the Poisson equation is solved accurately. The nonperiodic solver needs twice the grid size for padding the Fourier transforms. This limits the resolution of our simulations to effectively 512^3 cells.

2.5. Core Identification

We use two methods to identify cores in the model data. To find gravitationally bound objects, we employ the Clumpfind algorithm (Williams et al. 1994) in a modified version (Klessen et al. 2000). We then test whether the structures identified by Clumpfind are gravitationally bound or collapsing by checking their Jeans mass, the ratio of thermal and (internal) kinetic energy to gravitational energy, and the velocity divergence. If all three tests are passed, a structure is accepted as a core. We track individual cores by identifying the closest "neighbor" to a given core in the next time step (where "time step" does not mean the CFL time step, but the time between writing data sets). The simulations presented here form sufficiently few cores for this simple method to be accurate.

The second method is a simple clipping algorithm, motivated by the fact that due to the thermal instability, dense coherent regions are generally well defined in our models. The method selects the maximum density and builds a tree structure around the central cell, thus connecting all cells above the given density threshold of $n_{\text{th}} > 50 \text{ cm}^{-3}$. Once this threshold is reached, the process restarts with the next lower density peak not included in the previous structure. The resulting cores are accepted independently of whether they are gravitationally bound or collapsing.

3. MODEL RESULTS

The general signature of fast local fragmentation in colliding flows is most easily recognized in the morphologies of the clouds (§ 3.1). A more quantitative measure can be gleaned from the core mass evolution and the energy distribution (§ 3.2). Dynamical signatures are discussed in § 3.3, and § 3.4 sounds two cautionary notes regarding the numerical resolution.

3.1. Morphologies

We begin by comparing the morphologies of the clouds forming in colliding flows (models Hf1, Gf1, and Gf2; § 3.1.1). A new formation mechanism for massive cores is discussed in § 3.1.2.

3.1.1. Global Collapse and Filament Formation

The top row of Figure 1 shows three time instances of model Hf1, seen along the inflow direction. The colliding flows cause a big "splash," the effects of which are still noticeable 7.6 Myr after the initial flow collision (*left*); however, rapid cooling leads to strong density enhancements in the interaction zone and, in combination with the dynamical instabilities triggered by the perturbed interface, to strong fragmentation. Note the radial filaments and the outermost "bounding ring" at 7.6 Myr. The radial filaments are similar to those seen in the conceptually equivalent models by Vázquez-Semadeni et al. (2007): the compressed material is escaping the interaction region by the way of least resistance; i.e., laterally to the inflow. Once an "escape channel" has been formed due to small fluctuations in the external pressure, the resulting pressure deficit will ensure that the channel will continue to be used by subsequent material. The ringlike structure is just the shock wave from the initial splash caused by the colliding flows.

With increasing time, more and more mass is collected in the interaction region, rapidly assembling the cloud. Note that for the sake of greater detail, the middle and right columns of Figure 1 show only 3/4 (in linear extent) of the simulation domain, corresponding to a box length of 33 pc. The nongravitating model Hf1 also continues to collect mass as time proceeds; however, the column densities reached do not exceed a few times 10^{21} cm^{-2}.

This changes with the introduction of gravity (Fig. 1, *middle and bottom*). At 7.6 Myr, the structures are still pretty much indiscernible, while at 11.4 Myr, the first regions of high column density have formed. While the cores forming in the cloud result
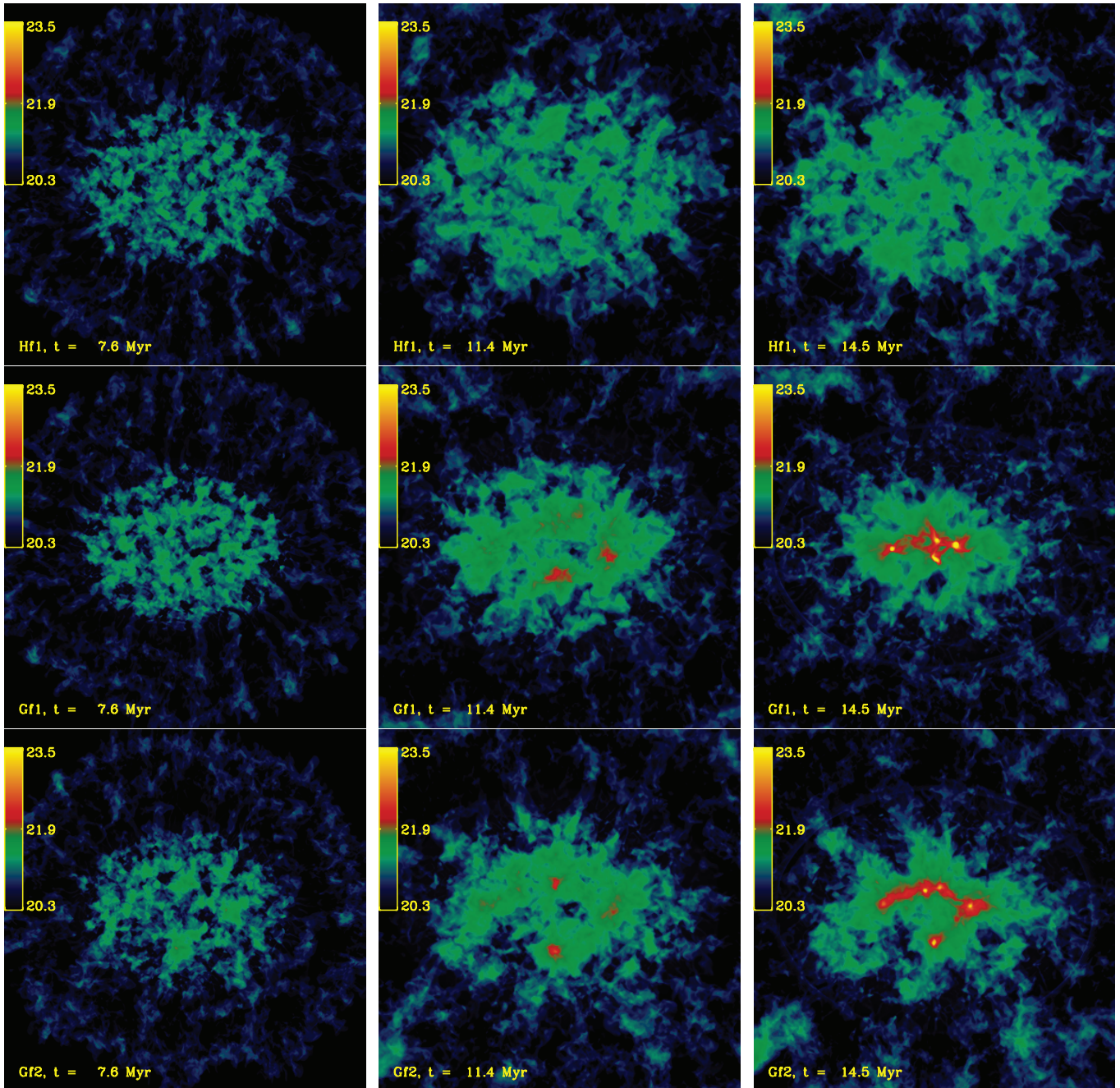
FIG. 1.—Time sequence of logarithmic column density maps for models Hf1 (*top*), Gf1 (*middle*), and Gf2 (*bottom*), seen along the inflow direction. At $t = 7.6$ Myr (*left*), the full domain (44 pc) is shown, whereas we restrict the field of view to the central 3/4 (33 pc) of the domain at later times, to highlight the small-scale dense structures forming.

from local collapse (see below), the filaments at later stages (14.5 Myr) are a consequence of the global collapse of the whole cloud. This can be more easily seen in the right column of Figure 2. The same models at the same times as in Figure 1 are shown, but they are now seen perpendicularly to the inflow. Clearly, at late times, the initially elongated red structure (the dense part of the cloud) crumples under its own weight. Because of the (generalized) noncircular inflow cross section, this leads to the formation of a filament. This mechanism for filament formation offers a substantial reservoir of mass for further star formation. The subsequent fragmentation of the filaments is possibly enhanced by the thermal instability (see, e.g., Tsuribe & Inutsuka 2001). The larger amplitude of the collision interface perturbation in model

Gf2 (see Table 1) leads to a stronger initial fragmentation, which is mirrored in a more distributed core formation at later stages.

Note that the high-density regions (in Fig. 1) do not necessarily form at the center of the cloud. On the contrary, there is a tendency for material to collect away from the center, forming filaments (see model Gf2 at 14.5 Myr), or at least extended dense cores. This is a mild version of the edge effect in collapsing finite sheets, as discussed by Burkert & Hartmann (2004) and as applied to a model of the Orion star-forming region by Hartmann & Burkert (2007). Figure 3 is more specific about the actual mechanism: it shows a map of the (projected) gravitational accelerations $|\nabla\Phi|$ in the midplane perpendicular to the inflow (to be compared to the bottom row of Fig. 1). Contours denote the
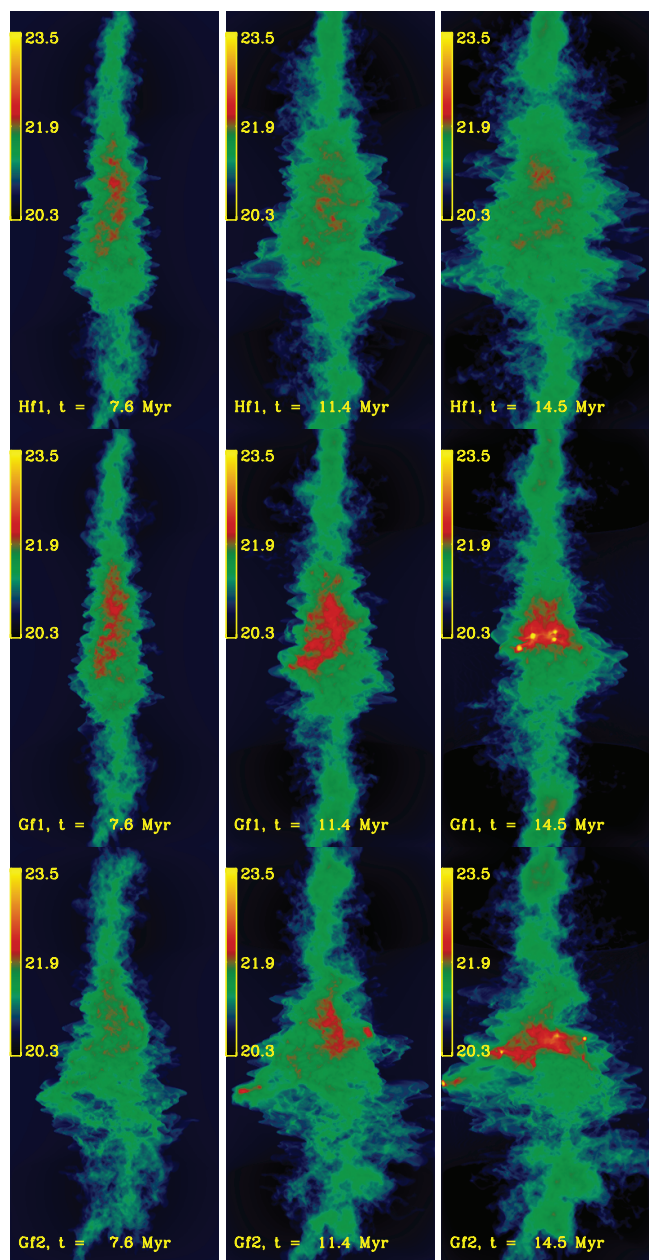
Fig. 2.—Time sequence of logarithmic column density maps for models Hf 1 (*top*), Gf 1 (*middle*), and Gf 2 (*bottom*), seen perpendicularly to the inflow direction. The full computational domain is shown, measuring 22×44 pc.

column density, and the actual potential gradient $-\nabla\Phi$ is indicated by the arrows. The color table is identical to Figure 1; i.e., yellow and red indicate strong accelerations. The ringlike structure of strong accelerations toward the center is obvious. Note that the accelerations extend toward larger radii than their accompanying high-density structures: material is accelerated at the edges and is being piled up further down the (radial) flow.

The simulations of Vázquez-Semadeni et al. (2007) show a similar effect to that of the models discussed here, although much stronger. This quantitative difference might be a consequence of the choice of initial perturbations in the two simulation sets. While Vázquez-Semadeni et al. (2007) put small-scale perturbations in their inflow velocities, we perturb the collision interface, which in turn leads to a stronger excitation of dynamical instabilities. The predominant instability arising in our setup is the nonlinear thin shell instability (NTSI; Vishniac 1994), in combination with

shear flow instabilities and the thermal instability (Field 1965), preventing the formation of a more or less uniform slab.

3.1.2. Dynamical Focusing and Massive Core Formation

The NTSI is driven by the ram pressure imbalance at the troughs of the rippled interaction surface: the concave side will have an excess of ram pressure because the flows are focused into the troughs, while the convex side will experience a deficit of ram pressure because the incoming gas is deflected. Thus, the NTSI provides a very efficient mechanism for collecting gas locally. Hueckstaedt (2003) demonstrated this effect with the help of self-gravitating two-dimensional models.

This focusing effect still holds in three dimensions, as can be seen from the time sequence of logarithmic column density maps of two colliding flows under the effect of self-gravity, as shown in Figure 4. The top left panel, at $t = 0.8$ Myr, shows structures that are still pretty close to the initial conditions. The cooling has not yet led to perceptible fragmentation, and turbulence has not yet developed. At 8.0 Myr, the NTSI is in full swing, and on the left edge of the cloud, roughly in the midplane, the first core starts to form. This core is located at one of the troughs amplified by the NTSI, so it has had ample opportunity to collect instreaming material. This seems to continue all the way up to 16 Myr, at which point the cloud has become globally unstable (see § 3.2), as indicated by the frenzy of core formation all over the cloud. We will present a more detailed discussion of the dynamical focusing in a subsequent paper, including models at higher resolution.

Isolating the gravitationally collapsing cores with Clumpfind (see § 2.5) and tracking the core masses with time yields Figure 5. The dynamical focusing seems to be a very efficient mechanism for collecting substantial mass in a small volume over a short time: at 9 Myr after the initial flow contact, the first 100 $M_\odot$ core has formed. At later times, the mass accretion rates get steeper: there is more mass available, and (concurrently) the potential well deepens, so that more massive cores can form within shorter times. The first core does not participate in the steepened accretion history because it sits at the edge of the potential well, so it does not benefit from the higher densities.

Obviously, stellar feedback will influence the cloud dynamics and star formation efficiency at late stages of the cloud evolution.

3.2. Collapse History

3.2.1. Energy Equipartition

A global measure for the cloud evolution under the effect of gravity is the equipartition parameter

$$\alpha_{\rm eq} \equiv \frac{\int \rho \boldsymbol{v}^2 + 3P \, dV}{\int \rho \Phi \, dV}, \qquad (2)$$

i.e., the ratio of the total kinetic and thermal energy over half the total potential energy.[5] We neglect any surface terms in the determination of $\alpha_{\rm eq}$, which only allows us to obtain a rough approximation of the true energetic state of the cloud. Nevertheless, as a close study of Figure 6 demonstrates, the time evolution of $\alpha_{\rm eq}$ mirrors the cloud morphologies (Figs. 4 and 1). Figure 6 shows $\alpha_{\rm eq}$ for all the gas above a given threshold density. A low

---

[5] We decided to follow Ballesteros-Paredes (2006) and avoid the term "virial parameter," since this usually has the connotation of virial equilibrium, an assumption that generally holds only for an ensemble of molecular clouds or for a time average of one cloud over many dynamical times (McKee 1999). Since we are concerned here with a single molecular cloud on short timescales, the notion of virial equilibrium is inapplicable, while that of energy equipartition may still hold (Ballesteros-Paredes 2006).
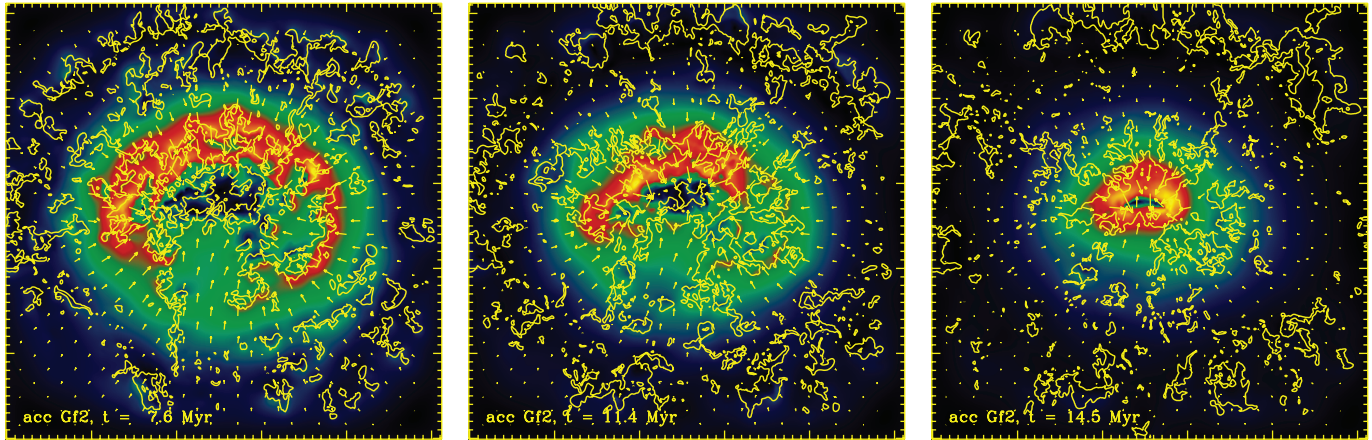
F$_{\text{IG}}$. 3.— Time sequence of accelerations for model Gf 2, projected in the plane perpendicular to the inflow. Colors denote $|\nabla\Phi|$, the contours represent density, and the arrows indicate $-\nabla\Phi$. This figure should be compared to the bottom row of Fig. 1.

threshold density means that most of the mass and most of the volume enter the calculation of α_{eq}. Increasing the density threshold emphasizes more and more the dense cores that form later. The lowest density threshold is set to $n_{\text{th}} = 10^2$ cm^{-3}, since we are interested in the equipartition parameter of the isolated cloud, and not that of the total simulation volume, including the (highly energetic) inflows. The following items are noteworthy:

1. The dense regions tend to be gravitationally bound ($\alpha_{\text{eq}} < 1$), while the global cloud behavior (illustrated by the lowest density curves) approaches $\alpha_{\text{eq}} \sim 1$ by the end of the simulations. Thus, in terms of observables, the cloud exhibits a value of α_{eq} consistent with virial equilibrium to within a factor of 2, which is well within observational uncertainties in terms of mass estimates, velocity dispersions derived only from line-of-sight motions, and the elimination of surface terms (Ballesteros-Paredes et al. 1999b; Ballesteros-Paredes 2006).

2. The solid lines indicating the lowest density threshold of $n_{\text{th}} = 10^2$ cm^{-3} reach $\alpha_{\text{eq}} = 1$ between 10 and 13 Myr. A lower

density threshold can be interpreted as tracing a larger volume; thus, the evolution of α_{eq} for low density thresholds indicates that global collapse lags behind the local collapse: isolated dense cores form before the cloud can collapse globally. However, the cloud does show the onset of global collapse.

3. At high density thresholds, $\alpha_{\text{eq}} < 1$ for all times (at which high densities are available): the massive cores (see the corresponding mass history) are fully gravitationally unstable. Note that α_{eq} does not drop further, although the mass increases: the cutoff of the cooling curve leads to a stabilization of the cores and prevents catastrophic collapse.

4. The clouds do not go through an equilibrium stage, but start to collapse locally during their formation: stars can form locally without a global collapse of the cloud.

Figure 6 allows us to make only an indirect statement about the scale-wise evolution of α_{eq}. A more accurate measure is the ratio of the respective Fourier spectra of the kinetic and internal energy over the gravitational energy. This yields $\alpha_{\text{eq}}(L)$, a scale-dependent measure of the cloud's stability against gravity (Fig. 7). As in Figure 6, we show the three gravitational models, but now at various times. Note that we do not select for gas in the cloud or gas above a density threshold. This is because masking leads to additional structure, which in turn results in noise signals in the Fourier spectra. To facilitate an easier comparison to spatial scales, we plot the scale-dependent quantity α_{eq} against the physical length scale, rather than against the wavenumber. Since α_{eq} is only a rough measure of the system's energetics, the following discussion should be seen as a qualitative analysis.

At early times, the system is gravitationally stable on all scales. This is not surprising, since we are now looking pretty much at the whole box (we removed the $L = 44$ pc mode, since this would just be the mean). The small scales definitely collapse first: they are the first to fall beneath $\alpha_{\text{eq}} = 1$ with increasing time. The minimum in α_{eq} at around $L = 1$–3 pc at earlier times stems from a conspiracy between the kinetic and potential energy scales: on larger scales ($L \gtrsim 3$ pc), the kinetic energy of the large-scale inflow still dominates the energy budget at early times, whereas on small scales, the potential energy drops faster with decreasing scale than does the kinetic energy. The small structures forming due to thermal and dynamical fragmentation have not yet had enough time to collect a significant amount of mass.

In summary, we note that in all models, local collapse wins over global collapse; i.e., the small scales generated by thermal and dynamical fragmentation collapse first. Global collapse, however,
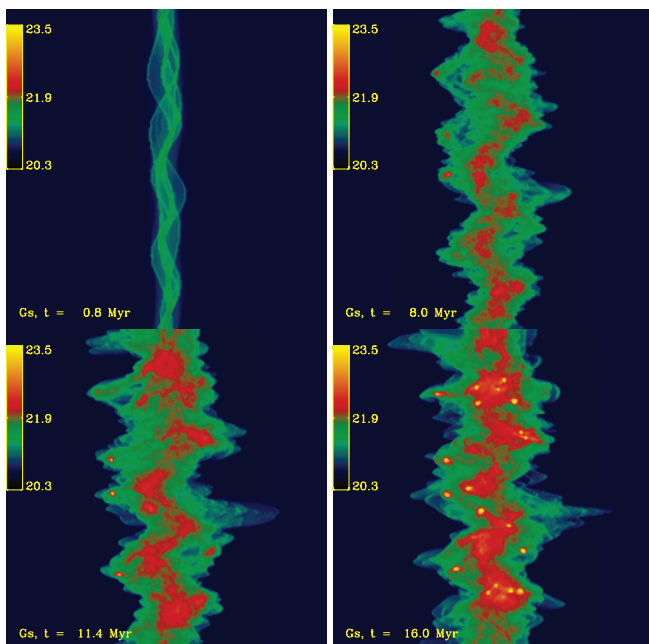

F$_{\text{IG}}$. 4.— Time sequence of logarithmic column density maps for model Gs, seen perpendicular to the inflow direction. The domain measures 44 pc in linear extent.
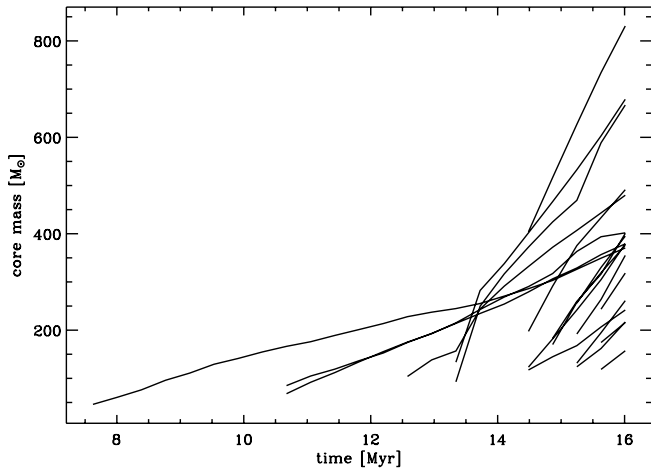
Fig. 5.—Core mass evolution for model Gs. The global collapse of the cloud is paralleled by a frenzy of core formation at late times.

occurs and feeds more material into the already active star-forming region. The clouds do not reach an equilibrium stage, but rather proceed from formation directly to local collapse and only then to global collapse. This result does not depend on the presence or absence of stellar feedback, in contrast to the late-stage evolution of our model clouds, where feedback will have a deciding influence.

3.2.2. Total and Core Mass Evolution

We have already seen the core mass history of model Gs (Fig. 5). Figure 8 shows the total mass evolution of all models. Thick lines refer to gas at $T < 100$ K, which can be identified as cloud gas due to the thermal instability. Thin lines denote the gas at $T > 100$ K. The symbols refer to the total mass within collapsing cores for each model; i.e., M_*, the mass that constitutes the reservoir for star formation.

Note that the mass is scaled logarithmically, while the (cold) cloud mass evolves linearly with time. Essentially, despite all the substructure, the colliding flows form one cold slab (see also Heitsch et al. 2006). If we compare models Hf1, Gf1, and Gf2, gravity does not affect the global cloud mass: the inflows determine the mass in the cold gas phase (i.e., in the cloud) and thus the material available for making stars. Model Gs differs from all

others just because of the larger extent of the collision site. Otherwise, its evolution regarding the cloud mass is qualitatively similar.

The core masses evolve nearly exponentially at times. This is a consequence not of the individual mass accretion events, as Figure 5 demonstrates; those are fairly linear with time. Rather, the nonlinear evolution is a consequence of the explosion of star formation activity once sufficient mass has been accumulated. Comparing the mass in the cores, M_*, against the cloud mass M_{cl} identified with $M(T < 100$ K$)$, we note that over a large stretch of time, the star formation efficiency $M_*/M_{cl} < 0.1$: the collapse is initially truly local.

3.2.3. Core Mass Distribution

Since the thermal instabilities are the first fragmentation agent in the colliding gas streams, will they set the core mass distribution in molecular clouds? Figure 9 shows the core mass distribution in logarithmic mass intervals for all four models. The (fit) slopes $d \ln N / d(\ln M) = s$ are indicated in the legend. The Salpeter initial mass function (IMF) would have an exponent of $s = -1.35$. While the slopes are approximately consistent with observed core mass distributions (Kramer et al. 1996; Schneider et al. 2002), we note that there is at most 1 decade in mass for the fits. Moreover, these mass spectra are most likely affected by the stiffening of the equation of state for $n > 10^5$ cm^{-3} (§ 2.3); i.e., low-mass objects may be underrepresented. This may cause a flattening of the spectra of the gravity models (Gf1, Gf2, and Gs), possibly visible in the bottom right panel (13 Myr) of Figure 9, whereas model Hf1 shows a rather well-defined power law down to the lowest masses at late times. Note that the cores contributing to Figure 9 are not necessarily self-gravitating. Over a period of 4 Myr, the spectra roughly keep their shape, another indication that the fragmentation is mainly due to thermal effects rather than to gravity.

3.3. Gas Dynamics

Figure 10 summarizes the various line-of-sight velocity dispersions (LOSVDs) for the cold ($T < 100$ K) gas, for all models. All LOSVDs are one-dimensional and density-weighted; e.g., the total LOSVD is

$$\sigma_v \equiv \left(\frac{\int v^2 n \, dV}{3 \int n \, dV} \right)^{1/2}. \qquad (3)$$
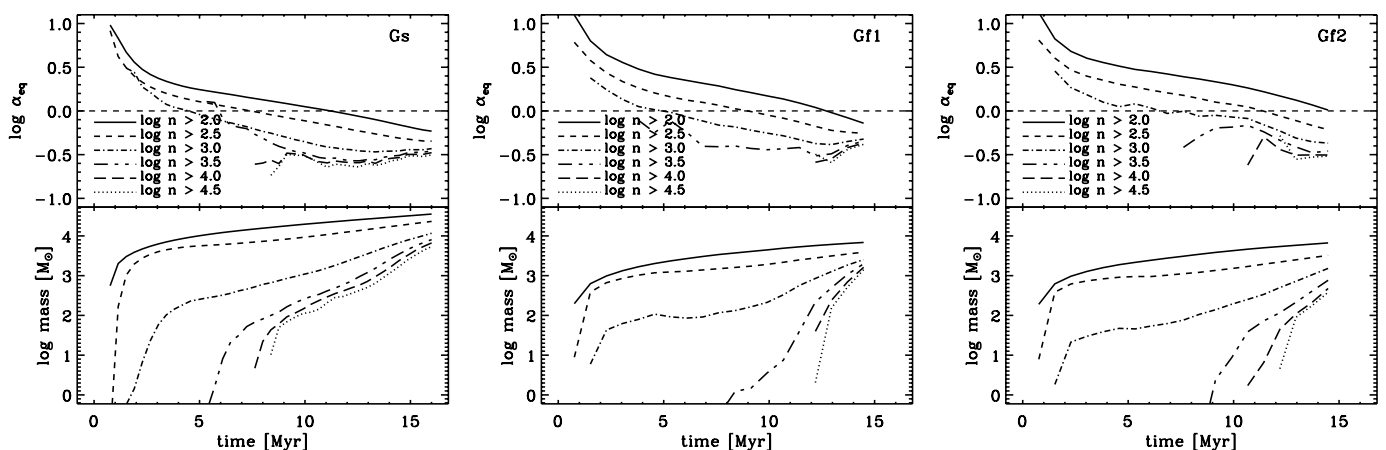

Fig. 6.—Equipartition parameter α_{eq} against time for the three gravity models Gs, Gf1, and Gf2, as indicated in the panels. The top half of each panel gives $\alpha_{eq}(n > n_{th})$, and the bottom half shows the total mass $M(n > n_{th})$. The line styles represent the threshold densities n_{th}, as indicated in the top panels.
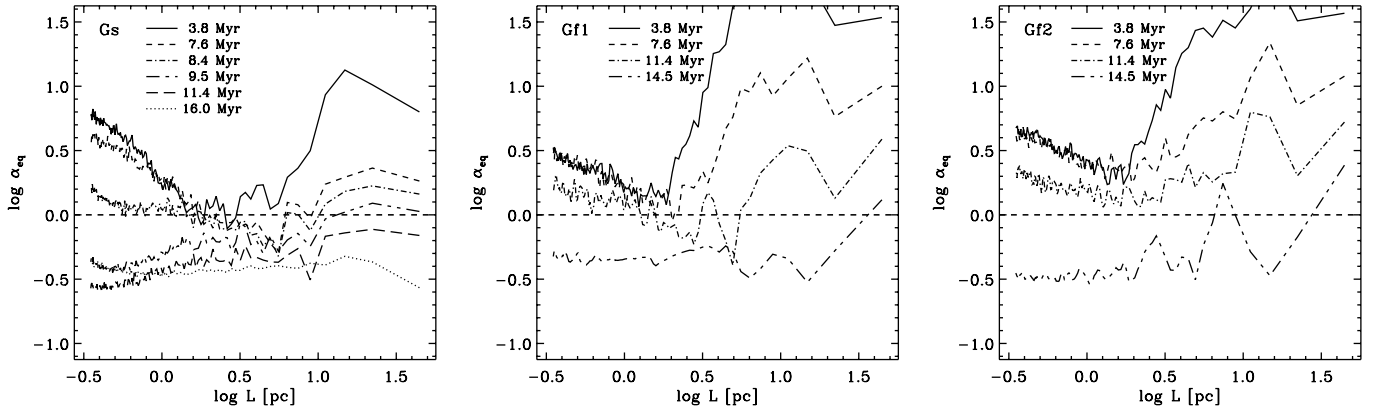
FIG. 7.—Equipartition parameter α_{eq} against scale for the three gravity models Gs, Gf1, and Gf2, as indicated in the panels. The line styles indicate the times at which α_{eq} has been measured. All models have been cut at a scale of 0.3 pc, although the numerical resolution is a factor of approximately 3 (6) higher for model Gs (models Gf1 and Gf2).

The top panel of Figure 10 shows the velocity dispersion along the inflow direction (σ_x), the transverse velocity dispersion (σ_{yz}) and the total dispersion. For all models, σ_x is highest, initially increasing slightly with time and later leveling off. The initial rise is due to the still-active NTSI; i.e., the ripples in the interaction interface are still amplified, while at later times the NTSI is saturated and global gravity takes over. The latter can be seen when comparing models Hf1 and Gf1, which are identical except that Gf1 has self-gravity. For both, σ_x initially evolves similarly, up to $t \approx 7.5$ Myr. After that, σ_x(Gf1) starts to level off, while σ_x(Hf1) still continues to rise: gravity constrains the slab and suppresses the further growth of the NTSI. This is obvious in Figure 2.

The transverse velocity dispersion σ_{yz} (lines of medium thickness in the top panel of Fig. 10) shows the influence of global gravity at later times for models Gf1, Gf2, and Gs, while that of model Hf1 drops with time. For model Hf1, the total energy input of the inflows is balanced by radiative losses and outstreaming material: the total velocity dispersion stays approximately constant with time. Not so for the self-gravitating models, which all have increasing total velocity dispersions with time.

In the bottom panel of Figure 10, the thick lines again represent the total velocity dispersion (as in the top panel). The thin lines ($\langle \sigma_{core} \rangle$) denote the velocity dispersion within each core,

averaged over all cores. This is the same quantity as the "internal" velocity dispersion as discussed by Heitsch et al. (2006). Due to the strong radiative losses, this velocity dispersion is subsonic (the sound speed in the cold gas is $c_s \approx 0.3$ km s^{-1}). In contrast, the velocity dispersion of all gas in the cores, σ_{core}, is slightly supersonic and increases with time due to global gravitational collapse.

3.4. *Two Comments on Resolution*

The left column of Figure 11 shows histograms of the Jeans length for all three self-gravitating models. The dashed vertical line indicates the Truelove et al. (1997) criterion with a safety factor of 4, mandating a minimum number of cells per Jeans length. We evaluate the criterion locally, i.e., per cell. Clearly, with increasing time, more and more cells fall below the resolution limit (to the left of the vertical dashed line). A more detailed view is offered by the set of panels on the right side of Figure 11. They show the Jeans length in each cell against the corresponding density. Again, dashed lines denote the Truelove limits, where the upper line shows the limit for 4 cells and the lower one shows the limit for 2 cells. Although only a minor fraction of the cells are unresolved, they do exist. The strict correlation between n and λ_J for $n < 10^5$ cm^{-3}, as well as the scatter at larger densities, is a direct consequence of the cooling curve: we are far up the isothermal branch, so the thermal timescales are much shorter than the dynamical timescales. As discussed above, we switch off the cooling for densities of $n > 10^5$ cm^{-3} in order to prevent unphysically high densities and subsequent numerical problems. The effective equation of state reverts to adiabatic with $\gamma = 5/3$ at that point, so the temperature increases due to the strong compressions.

There are several resolution criteria for thermally unstable systems (see, e.g., Hennebelle & Audit 2007 for a discussion). The dynamically most stringent condition is to resolve the cooling length, $\lambda_c = c_s \tau_c$. If this length scale is not resolved in the cold gas, the (isobaric) condensation mode of the thermal instability will be underestimated (see Field 1965 and Burkert & Lin 2000). The bulk of the cold gas resides at 40 K for our cooling curve (see Heitsch et al. 2006), and the cooling timescales in the cold gas are on the order of 10^4 yr, so the cooling length scale is $\lambda_c \approx 6 \times 10^{-2}$ pc, slightly beneath the nominal resolution for models Hf1, Gf1, and Gf2 (see § 2.1). Underestimating the condensation mode of the thermal instability will result in fewer low-mass fragments. In that sense, the core mass budgets (§ 3.2) and the fragmentation history in our models are conservative estimates: at
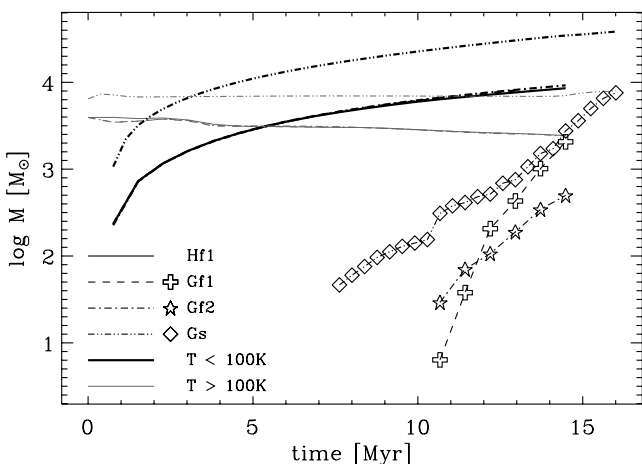

FIG. 8.—Mass history of all models. Thick lines denote $M(T < 100$ K), and thin lines denote $M(T > 100$ K). Different line styles represent the four models. Symbols refer to the total mass in collapsing cores identified by Clumpfind (see § 2.5).
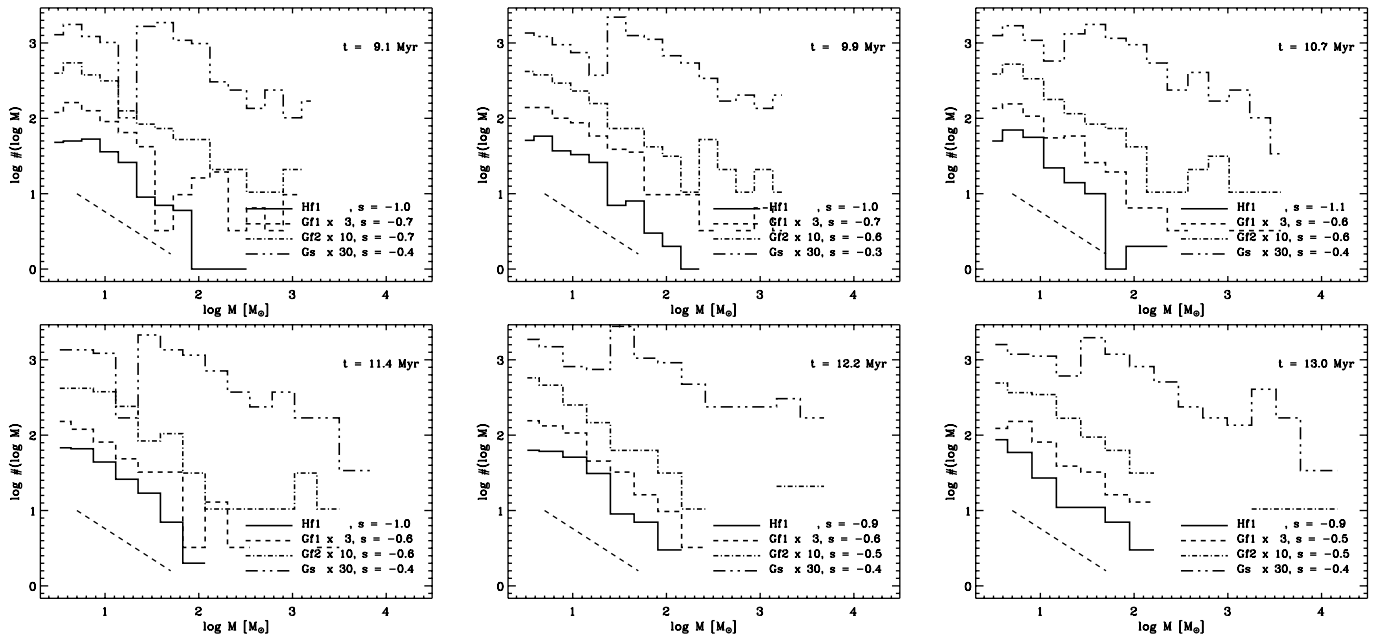
FIG. 9.—Time sequence of core mass distributions for all four models. Note that the distributions are shifted vertically by the factor indicated in the legend, to make them easier to identify. The Salpeter IMF would have a slope of -1.35. The dashed line denotes $d(\ln N)/d(\ln M) = -0.8$.

higher resolutions, more fragmentation, and possibly earlier low-mass star formation, is expected.

4. DISCUSSION

4.1. *Global Collapse and Filament Formation*

Galactic star formation seems to prefer filamentary, or at least elongated, rather than spherical molecular clouds (Schneider &

FIG. 10.—*Top*: One-dimensional velocity dispersions against time, along the inflow direction (σ_x; *thin lines*), in the direction perpendicular to the inflows (σ_{yz}; *medium lines*), and in total [$\sigma_v(T < 100$ K); *thick lines*], for all models. *Bottom*: One-dimensional velocity dispersions against time. We distinguish between the velocity dispersion within each core, averaged over all cores ($\langle\sigma_{\mathrm{core}}\rangle$; *thin lines*), the velocity dispersion of the gas taken over all cores (σ_{core}; *medium lines*), and the total velocity dispersion (as in top panel; *thick lines*).

Elmegreen 1979; Chini et al. 1997; Hartmann et al. 2001; Hatchell et al. 2005; Alves et al. 2007). The finite extent of the forming cloud opens two paths for filament formation. The first and obvious one is global collapse along the shorter axes. The second one, which is less obvious, arises from the fact that the radial accelerations in a two-dimensional elliptical or circular cloud of uniform density diverge at the edges. Thus, material at the edges experiences the strongest accelerations inward, leading to a piling up of gas at the edge, i.e., to the formation of a filament (Burkert & Hartmann 2004).

Obviously, real clouds are three-dimensional. However, if clouds form in (laterally constrained) colliding flows, they will have a finite extent and, more importantly, global gravity will not have had sufficient time to lead to a centrally peaked density profile. The strong thermal instabilities lead to an initially rather thin sheet, only broadened by the dynamical instabilities. Thus, to zeroth order, in such a scenario the sheet approximation is quite reasonable. The numerical models of Vázquez-Semadeni et al. (2007) and the global collapse pattern of models Gf1 and Gf2 above support this interpretation. In fact, the dynamical instabilities will enhance a "crumpling" of the cloud in the lateral directions once global gravity dominates. As the discussion in § 3.1.1 shows, however, stars will have formed locally by then.

It is reasonable to assume that the (idealized) inflows implemented in our models will not have a circular cross section. In galaxy mergers or in the collisions of supershells in the LMC, the thickness of the disk would limit the thickness (vertical extent) of the flow. A similar assumption seems to be valid for spiral shocks in the Galaxy, where the disk potential would again lead to a flattening of the inflows (e.g., Dobbs et al. 2006).

4.2. *Formation of Massive Cores*

Ripples in the flow collision interface can focus the in-streaming gas, leading to a very efficient mechanism for the formation of massive cores (Figs. 4 and 5). At 10 Myr after flow collision, the first core in model Gs has a mass of approximately 150 $M_{\odot}$ and a diameter of 1 pc, corresponding to a column density
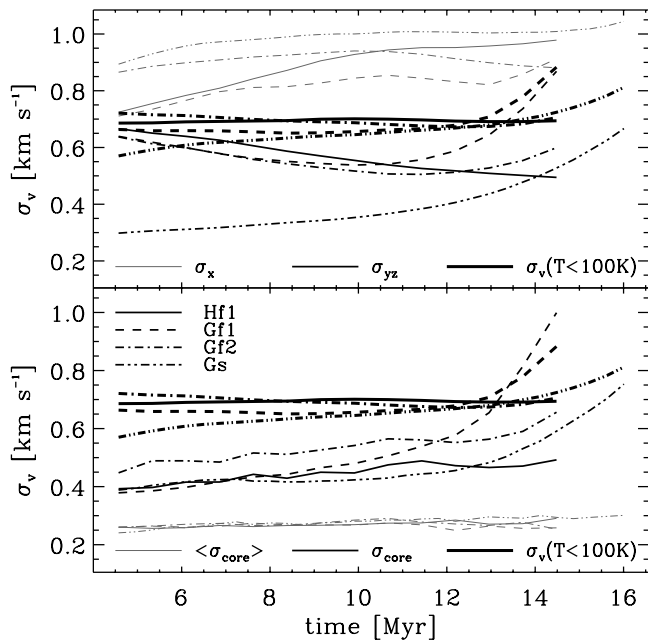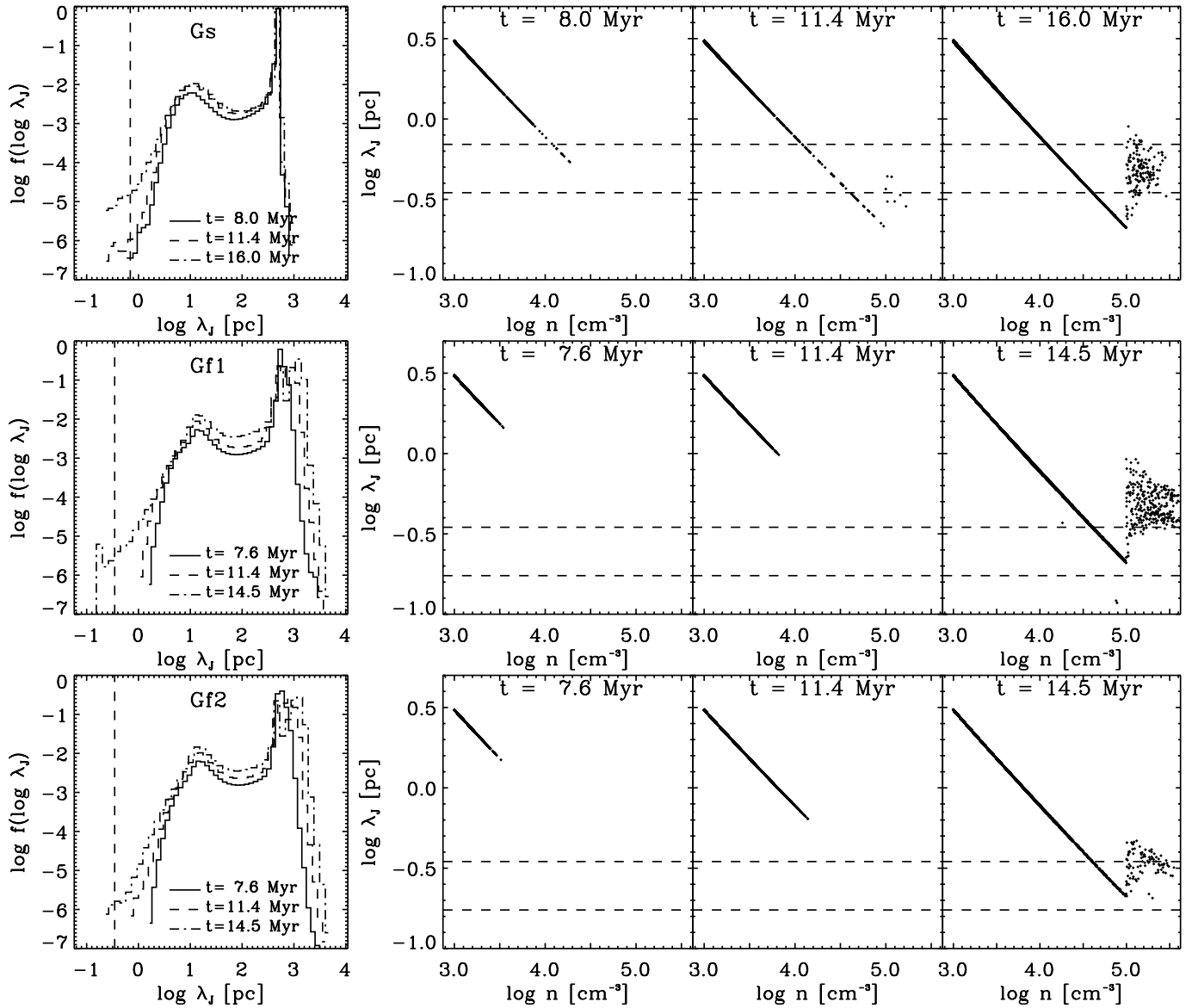
Fig. 11.—Histograms of the Jeans length (*left*) for all three self-gravitating models, and scatter plots of the Jeans length against density for all models at three times (*right*). The dashed lines denote the Truelove et al. (1997) criterion with safety factors of 2 and 4.

of 3.6×10^{22} cm^{-2}. Likewise, after 10 Myr, the mean column density in the box along the inflow direction will be $N_{tot} = (3$ cm$^{-3})[44$ pc $+ (7.9$ km s$^{-1})(10$ Myr$)] = 1.1 \times 10^{21}$ cm^{-2}. The dynamical focusing, helped along by cooling and eventually by gravity, leads to an excess of the column density by a factor of ≈ 30.

This is as good a place as any to remind the reader that we are leaving out the crucial step of molecule formation in our models. The first appearance of molecules sets the clock for the lifetime of the cloud. We can only mimic this by arguing that once column densities of $\approx 10^{21}$ cm^{-2} are reached, we regard the cloud as "molecular." Hartmann et al. (2001) point out that this column density is of the same order as the critical column density for gravity to become dominant.

With the NTSI as the driving mechanism, cores will form at a certain distance from the bulk of the cloud (Fig. 4). This distance is basically given by the amplitude that the NTSI has reached up to that point. The somewhat peculiar location could have profound repercussions on the effect of feedback from the massive stars forming in the core: the winds and the expanding H ɪɪ re-

gions or supernovae might lead to a further compression of the already massive cloud next to the young stars, thus triggering further star formation. In contrast, if the stars were located inside the bulk of the cloud, the stellar feedback could be expected to provide partial support to the cloud or, more likely, disperse the lower density regions.

Keto et al. (2005) analyzed the molecular cloud population of the starburst galaxy M82, arguing that in many cases, star formation seems to proceed from the outside inward; i.e., that the regions of massive star formation (indicated by H ɪɪ regions and supernova remnants) are to be found at the edges of the molecular clouds. They argue that a sudden increase in external pressure (e.g., a shock wave traveling through the cloud) triggers star formation in a previously existing cloud. The dynamical focusing effect discussed here might offer another explanation, which then would imply that the central molecular cloud is still forming, an alternative that may be even more attractive in view of the notorious problem of stabilizing an object of many Jeans masses against gravitational collapse (Burkert & Hartmann 2004; Ballesteros-Paredes & Hartmann 2007).

The role of the external pressure increase in our models is taken over by dynamical focusing; i.e., by the excess ram pressure at the troughs of the perturbed sheet. As Figure 12 demonstrates, the *thermal* pressure does not vary strongly. Thus, the gas still evolves subisothermally; i.e., the effective adiabatic exponent is $\gamma < 1$.

At late times (Fig. 12, *top*; 15.2 Myr), kinetic and gravitational pressure are in equipartition. Once again, we emphasize that this does not mean that the system is in equilibrium: the kinetic energy just follows the gravitational energy (Ballesteros-Paredes 2006).

4.3. *Early Fragmentation and Core Mass Distributions*

The core mass distributions (Fig. 9) are consistent with observations (Kramer et al. 1996; Schneider et al. 2002), although they are flatter than the Salpeter IMF. Alves et al. (2007) quote a core mass distribution for the Pipe Nebula that is close to the Salpeter IMF; however, as they point out, the cores that they are using for analysis are probably the direct progenitors of stars, a stage we cannot hope to reach with the models presented here. If we bear in mind that the distributions for models Gf1, Gf2, and Gs are probably slightly too flat for numerical reasons (§ 3.2.3), their similarity to the nongravitating model Hf1 substantiates the claim that the density substructure, specifically the core mass distribution, in molecular clouds could very well arise very early on during their formation (Alves et al. 2007; Hennebelle et al. 2007), driven more by thermal than by gravitational fragmentation.

However, we caution that we have not followed the cloud evolution through the stage of molecular hydrogen formation, an investigation we defer to a later paper. Finally, we again emphasize the difficulty of determining mass spectra from simulations with a limited dynamic range.

4.4. *Star Formation Duration and Stellar Age Spread*

From Figure 5, one would infer an age spread of the stellar population in the complex of up to 8 Myr. This of course assumes that massive, self-gravitating cores will sit around for several Myr without forming massive stars whose energy input will tend to disrupt the cloud: a highly improbable supposition. While this aspect of our simulation is quantitatively unrealistic, it does suggest the following qualitative points:

1. Even in a completely dynamic simulation without magnetic or driven turbulent support, the overall timescales of star formation can be longer than the local collapse times. Putting this another way, the age spread in a star-forming region is an *upper limit* to the timescale of local collapse; it is only equal to the local collapse time if all star formation is globally synchronized, which is less and less plausible on larger and larger scales.

2. The large-scale flow picture of star-forming cloud accumulation is attractive in that it allows for the formation of stars over timescales (1–2 Myr) that are short compared with lateral crossing times (10–20 Myr), as is observed (Hartmann et al. 2001). This does not mean that a region of space may not have a significant age spread. In the paradigm we are pursuing, in which nonlinear fluctuations are important, it is plausible that a few large perturbations might collapse long before more general star formation ensues, as we see in our simulations. Although our simulations form mostly massive cores, other initial conditions, and higher numerical resolution (see § 3.4), may lead to the formation of a few low-mass stars initially from the low-probability high-density tail of perturbations, with the smaller, more frequent perturbations constituting the bulk of the star formation at a later time. Again, such age spreads provide no constraint on local collapse timescales.
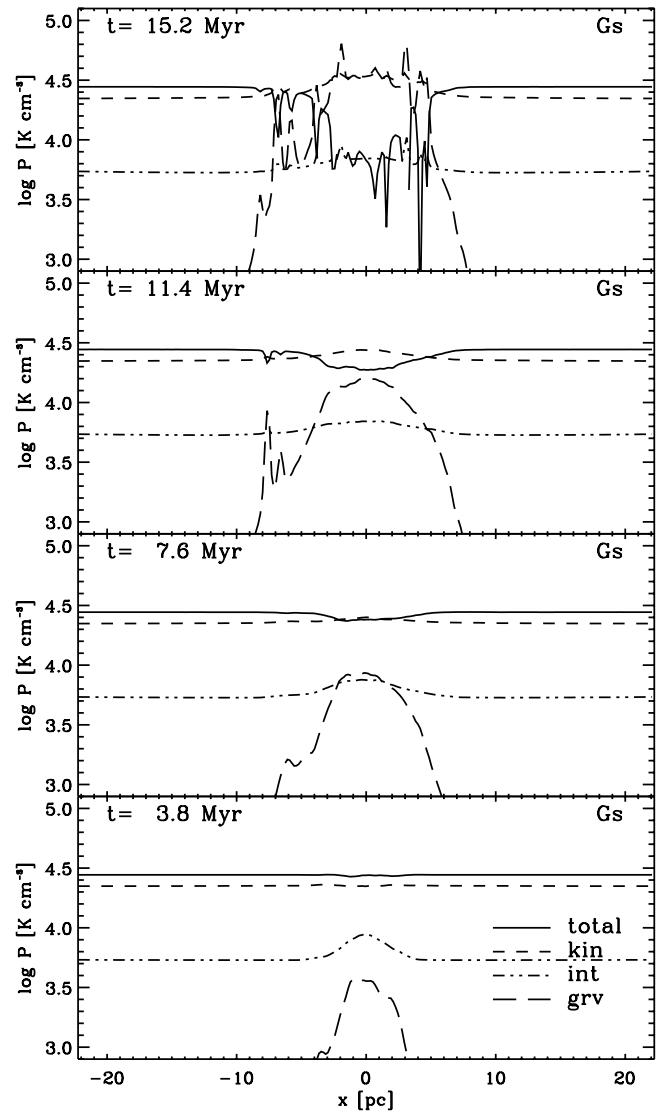

FIG. 12.—Laterally averaged pressure (energy density) profiles for model Gs, at times as indicated in panels. At 11 Myr, gravity has a noticeable global effect. Note that the internal pressure (*double-dot–dashed line*) varies only mildly.

4.5. *The Role of Magnetic Fields*

Magnetic fields are not included in the models presented here. On the basis of two-dimensional simulations by Vázquez-Semadeni et al. (1995), Hartmann et al. (2001) envisaged the large-scale converging flows preferentially running along (dynamically dominant; e.g., Heiles & Troland 2005) magnetic field lines in the diffuse ISM, arguing that if the field lines were oriented perpendicularly, the stiffening of the equation of state due to the increased magnetic pressure would counter the lowering of the effective adiabatic index due to (atomic line) cooling (see also Bergin et al. 2004). Although there are problems with this scenario (for one, substructures can form even in the case of perpendicular field lines and lead to further fragmentation [e.g., Heitsch et al. 2007], and then this scenario is clearly motivated by two-dimensional simulations, not allowing for interchange modes in the instabilities. These usually grow at least at the hydrodynamical rate; see, e.g., Stone & Gardiner 2007), we will adopt it for the current study. Its consequence is that since material is being piled up along the field lines, the mass-to-flux ratio would easily exceed the critical value for magnetic dominance (Mouschovias &

Spitzer 1976) after a few Myr, thus rendering the magnetic fields unimportant for the local gravitational collapse. It is true that the global dynamics of the cloud, especially during its early evolutionary stages, could be fundamentally influenced by the presence of magnetic fields. We will defer this important problem to a future paper.

5. SUMMARY

In an extension of our previous work (Heitsch et al. 2005, 2006), we have presented three-dimensional models of molecular cloud formation in colliding flows including self-gravity. At an effective resolution of 512^3, they currently are the most highly resolved models of this kind. We used a fixed-grid code and a nonperiodic Poisson solver. The initial conditions emphasized the effects of global versus local gravity on the newly forming cloud.

The model resolution did not allow us to follow the collapsed cores or to study their properties. Stellar feedback was not included. Thus, as time increases, the global evolution of the molecular cloud gets less and less realistic. Furthermore, we cannot make statements about the lifetime of the molecular cloud. With the caveats in mind, these are our results:

1. Any perturbation in the colliding flows is strongly amplified by a combination of thermal and dynamical instabilities. Specifically, the thermal effects lead to local high-density fragments that subsequently collapse before the (still forming) cloud can collapse globally. Thus, cloud formation in colliding flows allows the rapid onset of local star formation while evading the problem of globally collapsing clouds. This is consistent with earlier findings (Burkert & Hartmann 2004) that local collapse can only win over global collapse in the presence of early nonlinear density perturbations (Fig. 7).

2. Even in the highly dynamical environment of the colliding flows, an elongated finite cloud under global gravity can form one or more filaments by collapsing along its shorter axes. This lateral collapse opens up a further mass reservoir for star formation (Figs. 1 and 2).

3. Dynamical focusing, i.e., the deflection of incoming gas due to ripples in the interface between colliding gas streams, leads to very efficient high-mass core formation (Figs. 4 and 5): core masses of a few hundred $M_\odot$ are reached within ≈ 10 Myr.

4. The clouds are not in any state of equilibrium at any time. Different scales submit to gravitational collapse at different times, with the small scales going first (Figs. 6 and 7). Still, the global equipartition parameter (eq. [2]) ranges around 1 within a factor of a few, consistent with observations when taking into account the observational uncertainties.

5. The similarity of the core mass distribution for models with and without self-gravity and their robustness with time indicate that it might be set very early on during cloud formation. Thus, the core mass distribution would be a consequence of fragmentation due to (magneto)hydrodynamical instabilities and cooling rather than to self-gravity (Fig. 9).

6. The clouds become globally unstable in the absence of feedback, leading to an exploding "star formation efficiency" (in quotes, since we only can form cores in our models, not stars). The turbulence imparted by the (continuing) inflows is not sufficient to balance global gravity. As mentioned in § 1 and above, the absence of feedback in our models does not allow us to test how long the clouds will survive. However, our models show that the clouds will not disperse on their own accord in the background flows; i.e., without the help of stellar feedback.

REFERENCES

Alves, J., Lombardi, M., & Lada, C. J. 2007, A&A, 462, L17
Audit, E., & Hennebelle, P. 2005, A&A, 433, 1
Ballesteros-Paredes, J. 2006, MNRAS, 372, 443
Ballesteros-Paredes, J., & Hartmann, L. 2007, Rev. Mex. AA, 43, 123
Ballesteros-Paredes, J., Hartmann, L., & Vázquez-Semadeni, E. 1999a, ApJ, 527, 285
Ballesteros-Paredes, J., Vázquez-Semadeni, E., & Scalo, J. 1999b, ApJ, 515, 286
Bate, M. R., Bonnell, I. A., & Bromm, V. 2002, MNRAS, 332, L65
———. 2003, MNRAS, 339, 577
Bergin, E. A., Hartmann, L. W., Raymond, J. C., & Ballesteros-Paredes, J. 2004, ApJ, 612, 921
Burkert, A., & Hartmann, L. 2004, ApJ, 616, 288
Burkert, A., & Lin, D. N. C. 2000, ApJ, 537, 270
Chini, R., Reipurth, B., Ward-Thompson, D., Bally, J., Nyman, L.-A., Sievers, A., & Billawala, Y. 1997, ApJ, 474, L135
Dobbs, C. L., & Bonnell, I. A. 2007, MNRAS, 376, 1747
Dobbs, C. L., Bonnell, I. A., & Pringle, J. E. 2006, MNRAS, 371, 1663
Elmegreen, B. G. 2007, ApJ, 668, 1064
Field, G. B. 1965, ApJ, 142, 531
Gammie, C. F., Lin, Y.-T., Stone, J. M., & Ostriker, E. C. 2003, ApJ, 592, 203
Hartmann, L., Ballesteros-Paredes, J., & Bergin, E. A. 2001, ApJ, 562, 852
Hartmann, L., & Burkert, A. 2007, ApJ, 654, 988
Hatchell, J., Richer, J. S., Fuller, G. A., Qualtrough, C. J., Ladd, E. F., & Chandler, C. J. 2005, A&A, 440, 151
Heiles, C., & Troland, T. H. 2005, ApJ, 624, 773
Heitsch, F., Burkert, A., Hartmann, L. W., Slyz, A. D., & Devriendt, J. E. G. 2005, ApJ, 633, L113
Heitsch, F., Mac Low, M.-M., & Klessen, R. S. 2001, ApJ, 547, 280

Heitsch, F., Slyz, A. D., Devriendt, J. E. G., Hartmann, L. W., & Burkert, A. 2006, ApJ, 648, 1052
———. 2007, ApJ, 665, 445
Heitsch, F., Zweibel, E. G., Slyz, A. D., & Devriendt, J. E. G. 2004, ApJ, 603, 165
Hennebelle, P., & Audit, E. 2007, A&A, 465, 431
Hennebelle, P., Audit, E., & Miville-Deschênes, M.-A. 2007, A&A, 465, 445
Hueckstaedt, R. M. 2003, NewA, 8, 295
Keto, E., Ho, L. C., & Lo, K.-Y. 2005, ApJ, 635, 1062
Klessen, R. S., & Burkert, A. 2000, ApJS, 128, 287
Klessen, R. S., Heitsch, F., & Mac Low, M.-M. 2000, ApJ, 535, 887
Kramer, C., Stutzki, J., & Winnewisser, G. 1996, A&A, 307, 915
Krumholz, M. R., & Tan, J. C. 2007, ApJ, 654, 304
Mac Low, M.-M., & Klessen, R. S. 2004, Rev. Mod. Phys., 76, 125
McKee, C. F. 1999, in The Origin of Stars and Planetary Systems, ed. C. J. Lada & N. D. Kylafis (NATO ASI Ser. C, 540; Dordrecht: Kluwer), 29
McKee, C. F., & Ostriker, E. C. 2007, ARA&A, 45, 565
Mouschovias, T. C., & Spitzer, L., Jr. 1976, ApJ, 210, 326
Padoan, P., Juvela, M., Goodman, A. A., & Nordlund, Å. 2001, ApJ, 553, 227
Padoan, P., & Nordlund, Å. 2002, ApJ, 576, 870
Prendergast, K. H., & Xu, K. 1993, J. Comput. Phys., 109, 53
Schneider, N., Simon, R., Kramer, C., Stutzki, J., & Bontemps, S. 2002, A&A, 384, 225
Schneider, S., & Elmegreen, B. G. 1979, ApJS, 41, 87
Slyz, A., & Prendergast, K. H. 1999, A&AS, 139, 199
Slyz, A. D., Devriendt, J. E. G., Bryan, G., & Silk, J. 2005, MNRAS, 356, 737
Stone, J. M., & Gardiner, T. A. 2007, Phys. Fluids, 19, 094104
Tilanus, R. P. J., & Allen, R. J. 1990, in The Interstellar Medium in External Galaxies, ed. D. J. Hollenbach & H. A. Thronson, Jr. (SEE N91-14100 05-90; Washington: NASA), 298

Truelove, J. K., Klein, R. I., McKee, C. F., Holliman, J. H., II, Howell, L. H., & Greenough, J. A. 1997, ApJ, 489, L179

Tsuribe, T., & Inutsuka, S.-I. 2001, Ap&SS, 276, 1097

Vázquez-Semadeni, E., Gómez, G. C., Jappsen, A. K., Ballesteros-Paredes, J., González, R. F., & Klessen, R. S. 2007, ApJ, 657, 870

Vázquez-Semadeni, E., Kim, J., Shadmehri, M., & Ballesteros-Paredes, J. 2005, ApJ, 618, 344

Vázquez-Semadeni, E., Passot, T., & Pouquet, A. 1995, ApJ, 441, 702

Vázquez-Semadeni, E., Ryu, D., Passot, T., González, R. F., & Gazol, A. 2006, ApJ, 643, 245

Vishniac, E. T. 1994, ApJ, 428, 186

Williams, J. P., de Geus, E. J., & Blitz, L. 1994, ApJ, 428, 693

Wolfire, M. G., Hollenbach, D., McKee, C. F., Tielens, A. G. G. M., & Bakes, E. L. O. 1995, ApJ, 443, 152